In silico study of cuspid' periodontal ligament damage under parafunctional and traumatic conditions of whole-mouth occlusions. A patient-specific evaluation

Javier Ortún-Terrazas*, José Cegoñino, Amaya Pérez del Palomar

Group of Biomaterials, Aragon Institute of Engineering Research (I3A), University of Zaragoza, Zaragoza, Spain

ARTICLE INFO

ABSTRACT

Background and objective: Although traumatic loading has been associated with periodontal ligament (PDL) damage and therefore with several oral disorders, the damage phenomena and the traumatic loads involved are still unclear. The complex composition and extremely thin size of the PDL make experimentation difficult, requiring computational studies that consider the macroscopic loading conditions, the microscopic composition and fine detailed geometry of the tissue. In this study, a new methodology to analyse the damage phenomena in the collagen network and the extracellular matrix of the PDL caused by parafunctional and traumatic occlusal forces was proposed.

Methods: The entire human mandible and a portion thereof containing a full cuspid tooth were separately modelled using finite element analysis based on computed tomography and micro-computed tomography images, respectively. The first model was experimentally validated by occlusion analysis and subjected to the muscle loads produced during hard and soft chewing, traumatic cuspid occlusion, grinding, clenching, and simultaneous grinding and clenching. The occlusal forces computed by the first model were subsequently applied to the single tooth model to evaluate damage to the collagen network and the extracellular matrix of the PDL.

Results: Early occlusal contact on the left cuspid tooth guided the mandible to the more occluded side (16.5% greater in the right side) and absorbed most of the lateral load. The intrusive occlusal loads on the posterior teeth were 0.77–13.3% greater than those on the cuspid. According to our findings, damage to the collagen network and the extracellular matrix of the PDL could occur in traumatic and grinding conditions, mainly due to fibre overstretching (>60%) and interstitial fluid overpressure (>4.7 kPa), respectively.

Conclusions: Our findings provide important biomechanical insights into the determination of damage mechanisms which are caused by mechanical loading and the key role of the porous-fibrous behaviour of the PDL in parafunctional and traumatic loading scenarios. Besides, the 3D loading conditions computed from occlusal contacts will help future studies in the design of new orthodontics appliances and encourage the application of computing methods in medical practice.

1. Introduction

The stomatognathic system provides the complex function of chewing by the synergic activity of the elevator and depressor muscles that moves the mandible along the contact surfaces of the temporomandibular joints (TMJs) and that is limited by the occlusal surfaces of the teeth [1]. The occlusal reaction forces are meanwhile absorbed by the periodontal ligaments (PDLs) which play a key role in transferring them to the surrounding bone. Hence, PDL damage can result in a variety of disorders ranging from lesser to greater severity, including loss of the connective matrix, pathologic tooth movement, bone resorption, malocclusions, TMJ disorders, and myalgia [2,3]. Understanding the biomechanical

---

* Corresponding author at: Aragon Institute of Engineering Research (I3A), School of Engineering and Architecture, University of Zaragoza, Calle María de Luna 3, Zaragoza 50018, Spain.

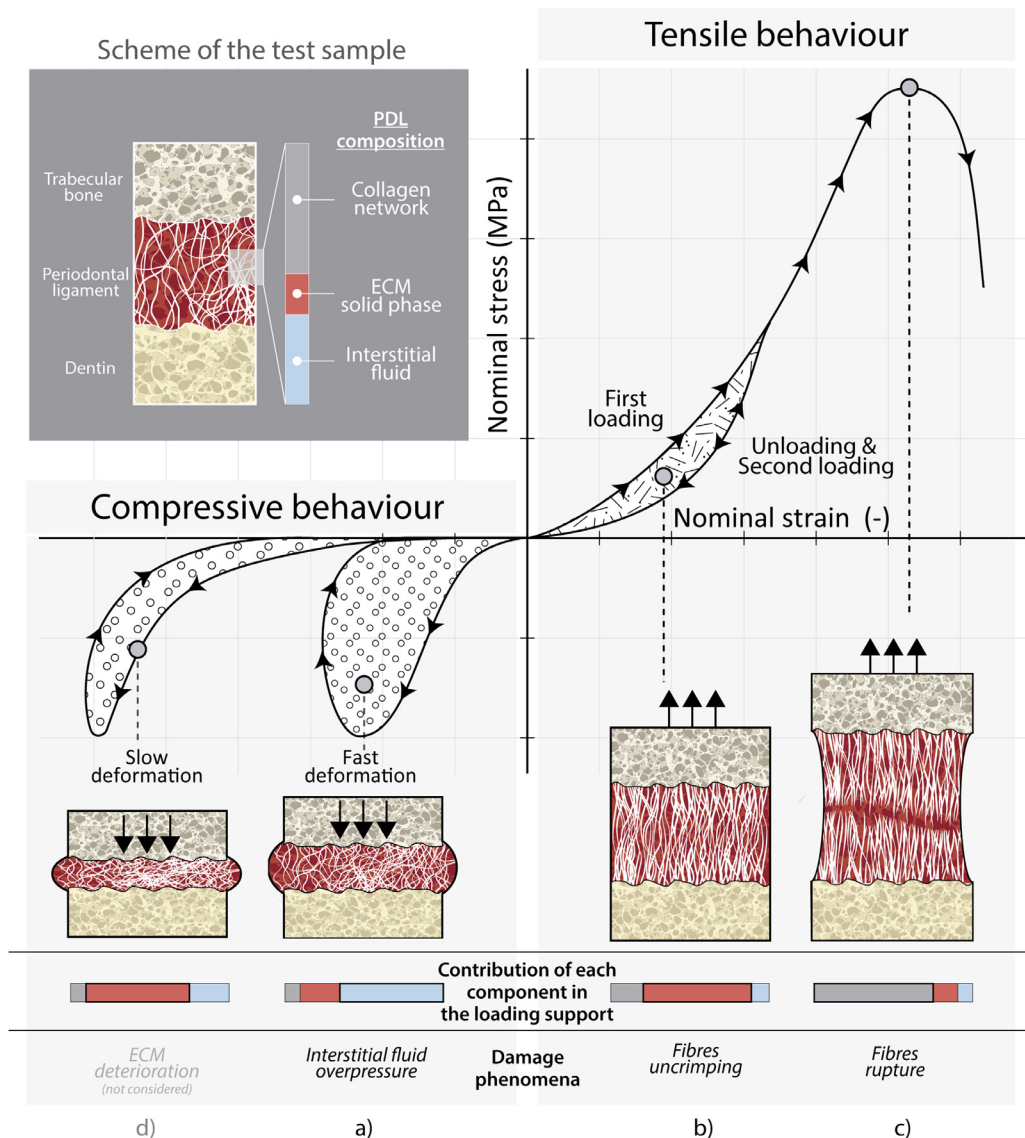*E-mail address:* javierortun@unizar.es (J. Ortún-Terrazas).

Fig. 1. Top grey box: tissue sample in relaxed state with crimped collagen fibres and scheme of the PDL composition. Below: an schematic showing an axial tensile-compressive test of a PDL until rupture with the representation of the fibres and the interstitial fluid of the tissue at different stages of the tension/compression test: a) tissue compressed with significant interstitial fluid contribution to the loading support; b) tissue partially stretched with fewer fibre entanglements and a high ECM solid phase contribution to the loading support; c) tissue overstretched and fibrous network almost completely ruptured; d) overcompression resulting in complete fluid extrusion and damage to the PDL's dry ECM. (This damage phenomenon was not considered in this study).

response of the PDL is crucial in order to elucidate its role in the development of these disorders [4–7]. Although several experimental [8,9] and computational [9–11] studies have attempted to describe the processes involved in PDL damage, it is still unclear how mechanical loading under traumatic and parafunctional conditions affects the health of the PDL. Moreover, study of the PDL is complicated by its complex mechanical and anatomical composition.

Anatomically, the PDL is a soft connective tissue composed of an extracellular matrix (ECM) in which a fibrous collagen network is embedded [12] and elastin fibrils are randomly distributed [13] (Fig. 1). The collagen network is mainly composed of collagen types I (approximately 80%) and III (about 15%), but also of types IV, V, VI, XII and XIV in small quantities [14]. The non-fibrous component of ECM is composed by lymph vessels, blood vessels and the ground substance which includes proteoglycans, glycoproteins, hyaluronan and mainly, the interstitial fluid (about 70% of

the ground substance) [14,15]. Biomechanically, the fibrous network architecture has a key role in the transversally isotropic tensile behaviour of the PDL [9,16], while the rest of the ECM components cause an almost viscous-hyperelastic isotropic behaviour. Elastin fibrils contribute to ECM consistency and the fluid phase of the ECM generates a viscoelastic response to compression, absorbing most of the compressive load [15–17]. The viscoelastic behaviour confers the ligament with an almost incompressible response at fast strain rates and a highly compressible behaviour at slow strain rates [16,18]. Furthermore, excessive compression or fast strain-rates can hinder interstitial fluid flow, leading to damage of the ECM (Fig. 1a) [19]. In the unloaded state, the collagen fibres are wavy and partially disorganized [9,11,20] (Fig. 1b). Stretching of the tissue results in progressive uncrimping and alignment of the fibres, leading to a stiffer PDL response when the fibres are geometrically aligned (Fig. 1b) [9,16]. Thus, if the tissue is unloaded and immediately loaded again, the fibre entanglements

become disentangled [10,21] and some fibres are ruptured [22], softening the tissue mainly at the toe region. The network's architecture plays, therefore, a key role in the fatigue behaviour of the network, as it was recently demonstrated in Dhume et al. multi-scale study [22]. When fibres are uncrimped and the tissue continues being stretched under its stretching limit, the tissue stiffness become almost linear due to fibre are already aligned and uncrimped. Any further stretching causes complete rupture of the tissue (Fig. 1c). In summary, fast compressive strain rates and cyclic loads/overstretching of the PDL can lead to progressive damage of the ECM and the collagen network, respectively.

These complex damage phenomena significantly complicate attempts to perform *in vivo* and non-destructive experimental analyses [23]. Fortunately, computational methods such as finite element (FE) analysis enable non-destructive evaluation of PDL damage. However, most FE models are simplified by assuming that tooth's occlusal forces are almost oriented along tooth's long axis; simplified PDL geometry; and homogeneous or non-time dependent behaviour of the PDL.

The assumption of tooth's occlusal forces almost aligned with the tooth axis is mainly due to that fact that current devices do not enable measurement of the direction of occlusal forces in 3 dimensions [24]. FE models that include accurate definitions of tooth surfaces and of PDL damping behaviour would allow successful computation of occlusal loads on the dentition of a specific patient. Some authors [25–27] have used micro-computed tomography (μCT) scanning to avoid simplifying the occlusal surfaces and to take into account the irregular thickness of the PDL. Although some computational studies have characterized the viscous [4,10,28,29], fibrous [5,9] or porous-fibrous [16] behaviour of the PDL, few have considered the softening caused by the disentangled of the fibres entanglements, the alignment of the fibres and the damage of the chemical crosslinks at low strains or the damage caused by the rupture of the tissue at higher strains [9,10,21]. Consequently, the relationship between PDL damage and mechanical overload in realistic traumatic conditions remains unknown. No previous *in silico* study has analysed the PDL damage response under different 3D loading scenarios, taking into account the non-uniform thickness, the porous-fibrous structure of the PDL and the damage phenomena to which it was subjected.

In this study, we evaluated the mechanical response of the PDL and the damage it sustains when subjected to normal, parafunctional, and traumatic occlusal forces using an *in silico* approach that considers the 3D loading conditions, micromorphology, and porous-fibrous biological composition of the PDL through models of different scales. To this end, a FE model of a full dentition was subjected to various combinations of muscular forces that produced different occlusal conditions. Next, the occlusal responses gathered from the full dentition model were applied to a single tooth model of the left cuspid with fine detail that took into account the non-uniform thickness and porous-fibrous structure of the PDL and the damage phenomena to which it is subjected.

2. Material and methods

2.1. FE model of the full dentition

A 3D model of a complete dentition was developed from data of a 44-year-old male with a functional crossbite but with no periodontal diseases and with no facial asymmetry (chin deviation < 4 mm from the facial midline). The data was obtained as a part of an orthodontic treatment planning for the correction of the malocclusion and to push forward the left lateral incisor of the superior arch. It was digitalized by cone beam computed tomography (CBCT) (Vatech PaX-i 3D Green, Vatech Spain) using a 90-kVp tube voltage, tube current of 4 mA, field of view (FOV)

of 20 cm × 19 cm, an acquisition time of 24 s and a voxel size of 0.6 mm. The images were output in a 14-bit grey scale and 16,384 shades of grey. The cylindrical reconstruction of the dataset consisted of 210 images with an interscan distance of 0.60 mm. The hard tissues were automatically segmented by Mimics software (Mimics, v.19.; Materialise, Leuven, Belgium) using threshold levels of 226 [30] and 1688 [31] Hounsfield unit (HU) for osseous and dental regions respectively .The PDL was defined as a 0.2-mm-thick layer around each tooth [32,33] (Fig. 2a). Next, the model was meshed via a mesh convergence process using 1,120,179 elements in Abaqus software (Abaqus 6.14, Simulia, Rhode Island, USA).

Linear elastic properties were assigned to all tissues, except for the PDLs of this model, to which non-linear hyperelastic properties [34] were assigned (Table A.2). In the full dentition model, the porous fibrous properties were not considered for the definition of PDLs' behaviour in order to avoid excessively increasing the computational cost in Abaqus. Whereas in the single tooth model which will be later explained, porous and fibrous properties were considered.

The upper nodes of the maxilla were fixed, and the nodes of the condyles were linked to the point at which both condylar long axes are intersected (point P in Fig. 2a) by rigid beam elements. Although the displacements of this point were fixed, the beam elements could rotate, allowing the rotation of the mandible along the condylar axes, following the TMJ fulcrum theory [35]. By contrast, the condylar paths were neglected since the slight translation of the condyles from the initial position of the mandible (resting position) to its position in centric occlusion (CO). The occlusal contacts were defined using a friction coefficient of 0.2 [25,36], and a penalty contact formulation. The PDLs were attached to the surrounding hard tissues by tied connections. Multiple loading conditions were simulated: hard and soft normal chewing by the right side (chewing side in Fig. 2a), traumatic cuspid-cuspid occlusion, and parafunctional conditions (grinding, clenching, and a combination of both). For each loading condition, the masticatory muscles were mimicked by connector elements that simulate the passive, active, and dampening responses of the muscles. To simulate hard and soft chewing tasks the muscles activation data of the study of Farella and coworkers [37] was used, when a piece (1 × 1 × 1 cm) of dried meat and a commercially available gum (Spearmint, Migros, Zurich, Switzerland) were respectively chewed. In the occlusal trauma simulation, only cuspid-cuspid contact was allowed.

To compare the simulation with a real voluntary clenching scenario, the patient's occlusion was experimentally recorded by piezoelectric film sensor using a T-Scan III system (Tek-Scan South Boston, MA, USA) and visualized in T-Scan v10 software. The occlusal contacts of the simulation were then compared with the experimental measurements in a common visualization environment. Additional information on the mesh, material properties, muscle forces, and occlusal analysis is provided in Appendix A.

2.2. FE model of the single cuspid tooth

A portion of a human mandible with the entire left cuspid was scanned *ex vivo* using a μCT scanner (Skyscan 1172, Bruker μCT N.V., Kontich, Belgium). The resulting tomographic images were re-built using a modified Feldkamp algorithm in NRecon 1.6.1.7, applying reduced artifact. The model was meshed in Abaqus using 267,913 elements (Fig. 2b).

In contrast to the FE model of the full dentition, the porous-fibrous component of the PDL [16] was accounted for by means of a porous transversally isotropic hyperelastic material model, which also incorporated damage phenomena caused by fibre uncrimping and rupture [21]. The fibres were distributed cylindrically using a cylindrical coordinate system with the Z-axis running along
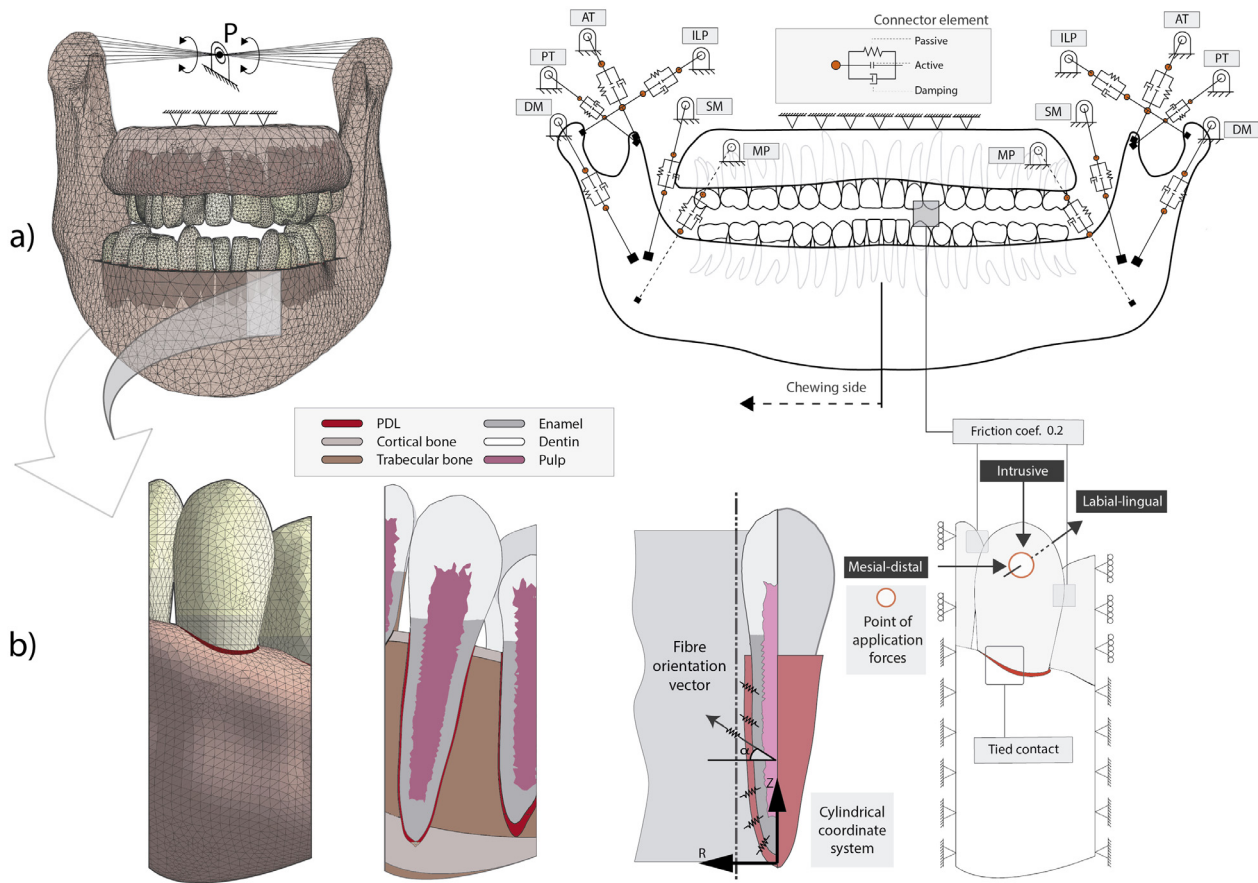
Fig. 2. a) Left: mesh of the full dentition model obtained by CBCT scan with mandible, maxilla, teeth, and PDLs. Right: schematic showing the boundary conditions applied to the model and the muscle system modelled. SM, superficial masseter; DM, deep masseter; ILP, inferior lateral pterygoid; AT, anterior temporalis; PT, posterior temporalis; MP, medial pterygoid. b) Left to right: mesh of the portion of a human mandible obtained by μCT; section of the model with color-coded components; schematic showing of the cylindrical coordinate system used to describe the orientation of the fibres bundles, and boundary conditions applied to the model.

the length of each tooth (Fig. 2b). For each fibre bundles, apical, oblique, horizontal, and alveolar crest, the preferential direction of the fibres (α vector in Fig. 2b) was defined varying α along Z-axis between 0 to −20, −20 to 55, 55 to 0, and 0 to 60° for each fibre bundles respectively, in accordance to a previous study of the literature [38]. Porous behaviour was also considered in the dentin and trabecular bone regions. The remaining tissues were defined using only elastic or hyperelastic properties, without considering viscoelastic effects. Additional information on the model, the validity of which has been previously demonstrated [16], is provided in the Appendix C.

To mimic the boundary conditions of the full mandible, the nodes located in the cutting planes of the mandible were fixed, and the movement of the cut surfaces of the lateral teeth was constrained to the mesial-distal direction (Fig. 2a). The properties of the occlusal contacts and the occlusal forces of the full dentition model were mirrored in this model. To establish the loading conditions, the occlusal reaction forces on the lower left cuspid tooth of the full dentition model were deconstructed into intrusive, labial-lingual, and mesial-distal components. The single tooth model was then loaded two times with these reaction forces with an unloading period of 1.12 s (sec) between each loading (show "opening" interval in Fig. 3b). Based on T-Scan measurements, normal chewing cycles were simulated for 1.58 s and maintained for 2.76 s to simulate parafunctional clenching (Fig. 3b). Grinding cycles lasted 0.95 s (Fig. 3c). To simulate spontaneous trauma, load was applied 25% faster than in hard and soft chewing tasks (2.70 s), in which the load was applied in 1.58 s and was removed in 1.12 s [39].

3. Results

3.1. Occlusal contacts

The occlusal analysis yielded quantifiable contact pressures for each tooth when the patient clenched with maximum voluntary force. Initially, the contacts predominantly centred on the left lower cuspid, guiding the mandible to the right (Fig. 3b). Posterior occlusion mainly occurred in teeth 16–17 and 26–27 (Fig. 3a). The full occlusion cycle ended with slightly greater loading on the right than the left side (58.2 and 41.7% of the total reaction forces, respectively) (Fig. 3a). The FE simulation yielded a similar occlusal pattern (Fig. 3a), with early contact on the left cuspid tooth (Fig. 4e) that guided the mandible slightly to the right.

3.2. Occlusal forces

Fig. 4 shows the reaction loads on the lower left cuspid and the premolars and molars of the right-hand side for different loading conditions. All simulations revealed an early cuspid-cuspid contact that decreased when the posterior teeth occluded, expect in occlusal trauma where posterior teeth did not contact. In hard and soft clenching tasks, the tangential friction on the cuspid tooth was maximum at the beginning of loading and decreased when the mandible was guided to the chewing side and posterior teeth began to occlude. Thus, the tangential friction forces on the posterior teeth were more uniform than on the cuspid tooth due to the excursive movement decreased and the occlusion is more stable at the end of the chewing cycle.
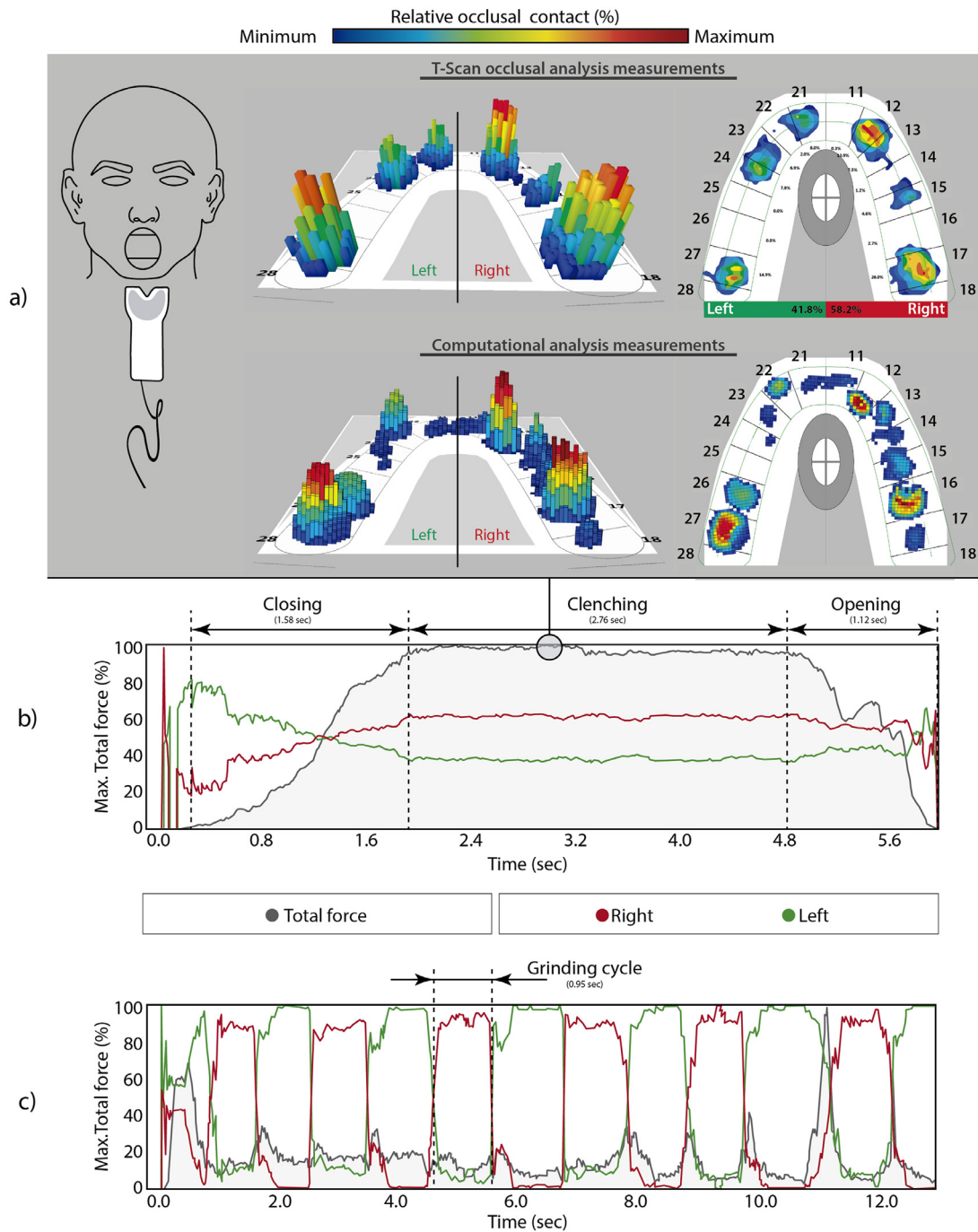
Fig. 3. a) Occlusal contacts at maximum intercuspation (MI) clenching measured by T-scan occlusal analysis sensor (top) and in a computational simulation (bottom), with maximum occlusal loads in teeth 16–17 and 26–27. Evolution of the relative percentage of the total occlusal force (black line) produced by the contacts on the teeth of the right (red line) or left (green line) dentition halves during clenching (b) and grinding (c).

In the 2 normal chewing scenarios (Fig. 4a and b), the normal reaction forces on the cuspid tooth were lower than 9 N and ranged from 17 to 120 N for the posterior teeth. The low tangential friction between posterior teeth may have been due to the fact that the lateral movements were mainly supported by the cuspid.

Maximum reaction force in the cuspid was obtained when traumatic loads were applied (Fig. 4c). In this loading scenario, 2 different slopes were observed: the first was caused by sliding of the upper canine along the mesiolingual fossa of the lower cuspid. The second slope occurred when the mesial cusp ridge of the lower cuspid contacted with the cingulum of the upper cuspid.

During grinding movement, the reaction forces on the cuspid tooth were more than 3 times greater than normal occlusal reaction forces (Fig. 4d), but were similar to those observed for clenching (Fig. 4e), during which most of the occlusion was supported by the posterior teeth.

3.3. PDL reactions

Occlusal forces (black lines in Fig. 5) were applied twice to the single tooth model to induce a reaction movement (grey discontinuous lines in Fig. 5) of the cuspid tooth for each loading.
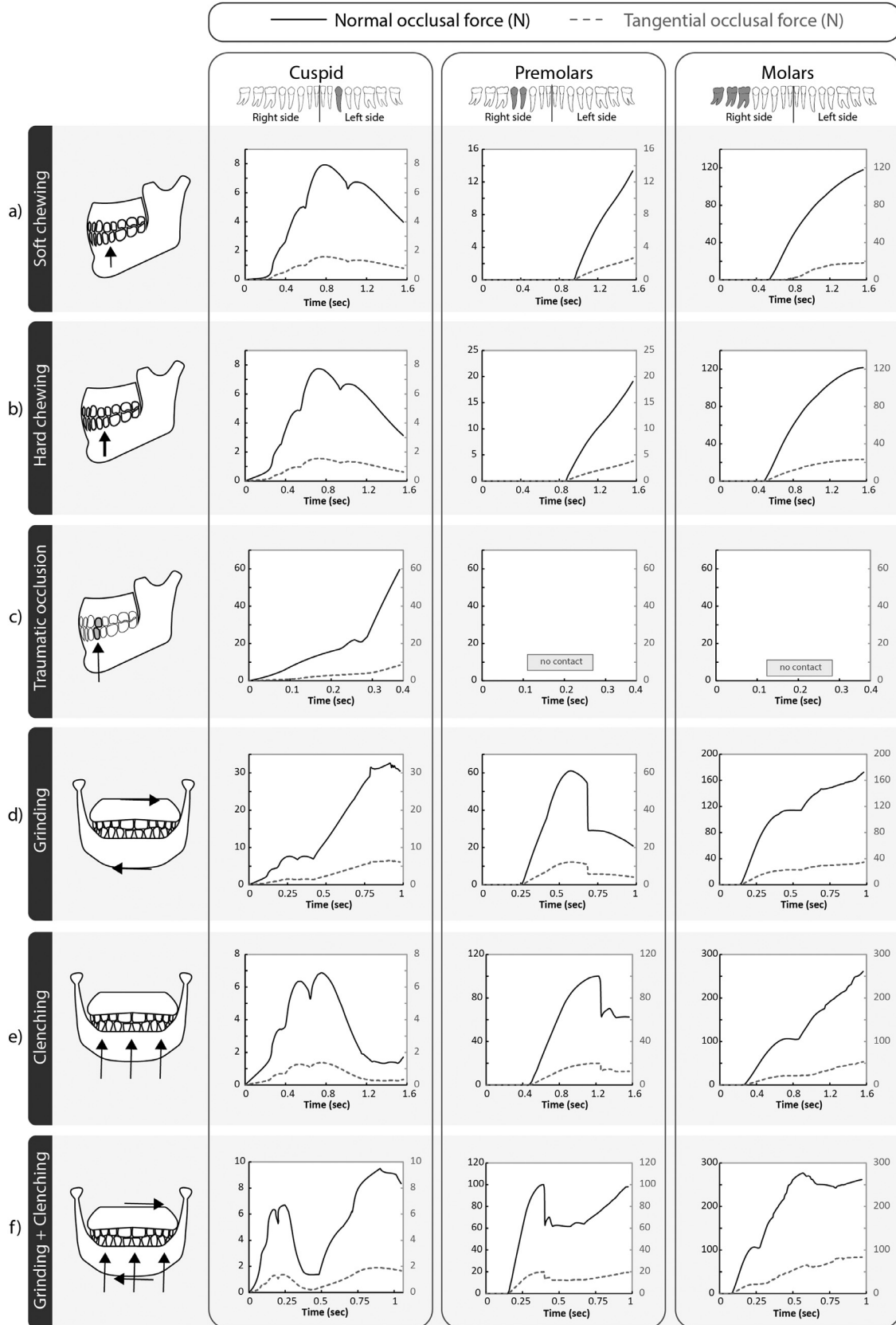
Fig. 4. Normal (black lines) and tangential (grey discontinuous lines) occlusal forces on the left cuspid, both right premolars, and the 3 right molars during a) soft chewing; b) hard chewing; c) traumatic cuspid-cuspid occlusion; d) grinding; e) involuntary clenching; and f) combined grinding and clenching.

Fig. 5. Deconstructed vectors (black lines) of the occlusal force gathered from the cuspid tooth in the full dentition model and resulting displacement (grey discontinuous lines) of the cuspid tooth in intrusive, labial-lingual, and mesial-distal directions during a) soft chewing; b) hard chewing; c) traumatic cuspid-cuspid occlusion; d) grinding; e) involuntary clenching; and f) combined grinding and clenching.

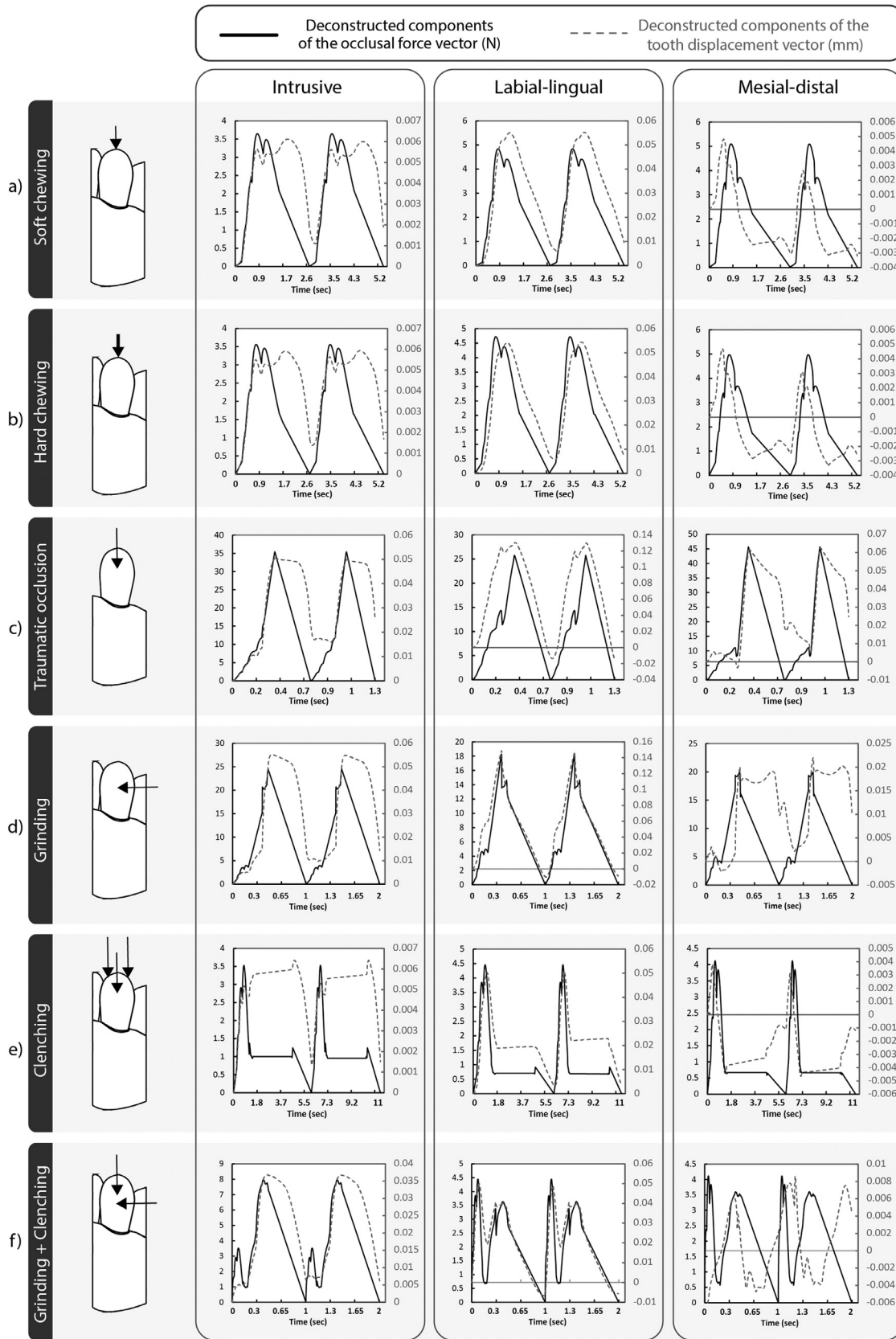Remarkably, the residual displacements observed after the first cycle due to the combination of the viscous effect of the fluid phase with the softening phenomena of the fibre uncrimping.

Normal chewing forces (Fig. 5a and b) cause the cuspid tooth to rotate, leading to compressive loads in the alveolar-crest and in the apical regions of the bone in distal and mesial directions, respectively (Fig. 6a and b). These compressive loads resulted in energy dissipation (third column in Fig. 6a and b) and therefore an increase in hydrostatic pressure (Fig. 7a and b) due to fluid flow in these areas. Nonetheless, overstretching of the fibrous network only occurred when traumatic loads were applied (Fig. 5c). Damage of the fibrous network (Fig. 6c) resulted in an abrupt increase in fluid overpressure (Fig. 7c) at the 80–100% of the first loading cycle which correspond to the 0.32–0.40 s time period. On the other hand, excessive tooth rotation in response to grinding (Fig. 5d) resulted in local stress distribution on the alveolar bone (Fig. 6d) and an interstitial fluid pressure (Fig. 7d) that was greater than the capillary blood pressure $\bar{\sigma}_h = 4.7 \ kPa$ (35mm Hg), which is considered by some authors [19,40] as the limit of the non-damage state. Curiously, no damage or overpressure phenomena occurred in the PDL when clenching loads were applied (Figs. 5d and 6e). Support of most of the occlusal forces by the posterior teeth likely explains the low stress state observed in these scenarios.

4. Discussion

PDL damage plays a key role in the development of many oral diseases, occlusal disorders, and the loss of bone and teeth [41]. Despite great effort by researchers studying the biomechanical responses of the PDL [9,15,21,23], the mechanisms underlying PDL damage remain unclear. Most previous studies have failed to adequately simulate the biomechanical response of the PDL by neglecting its irregular thickness and porous fibrous structure, or the variable direction of the tooth's occlusal forces during the mandibular movement.

In this *in silico* study, we studied porous-fibrous damage phenomena in the PDL using a fine detail model of a single tooth that was subjected to 3D normal, traumatic, and parafunctional loads that were first evaluated in a larger sized FE model of a full dentition.

The literature reveals several discrepancies regarding the magnitude of occlusal forces to which the PDL is subjected, with reported values ranging from 1 N [6,42,43] to over 100 N [44–46] for the same tooth. This lack of consistency is mainly due to patient-specific variations in number of contacts and the type of chewing activity analysed. Moreover, most studies do not consider viscoelastic phenomena. In the present study, we computed the magnitude and duration of occlusal forces using a macroscale model of a full dentition of a specific patient. The results of the occlusal analysis revealed a close correspondence between the computational findings and the contacts measured experimentally during clenching, with slight differences observed for the occlusion of premolar teeth on the right side (Fig. 3a) which could be caused by variations in the film' position or by tongue movements. Additionally, the gaps in the T-Scan measurements could be the result of a coarse adjustment of the device sensitivity since they coincide with the less occluded regions, or because an excessively soft material was used to simulate the film in the computational analysis. A previous study in which occlusion was analysed using T-Scan measurements [47] reported reliability errors of 2.8%. Possible explanations for the differences between our T-Scan measurements and the results produced by the model include the activation of different muscles in physiological versus modelled scenarios and deviations that may arise during image segmentation and modelling. Despite these differences, our simulations successfully mimicked the occlusal pattern, with an early

contact on the left lower cuspid (Fig. 4) that partially guided the mandible to the right (Fig. 3b). This occlusal pattern is a key feature of canine protected occlusion (CPO) [48], the main premise of which is that only cuspid-cuspid contact occurs during excursive movements of the mandible, and therefore that cuspid occlusion protects the posterior teeth from lateral loads. The T-Scan data (Fig. 3b) showed that the cuspid tooth plays a key role in orienting the mandible towards maximum intercuspation position at the beginning of the chewing cycle (0.8 s). When the occlusal reaction force was decomposed into the intrusive, labial-lingual, and mesial-distal directions (Fig. 5), it was noted that the occlusal force on the cuspid tooth was mainly applied laterally (labial-lingual and mesial-distal), promoting the tooth rotation around its centre of rotation (CR) [49]. The PDL stress values produced by our model were significantly higher than those reported in previous studies [50–52], in which the lateral directions of the tooth's occlusion force vector were not considered.

As expected, no signs of collagen network damage or ECM overpressure were observed in normal chewing conditions. However, in traumatic occlusion conditions damage of the fibrous network was caused by the high occlusal load in the intrusive direction ($>$ 60 N), resulting in partial rupture of the collagen fibres and interstitial fluid overpressure in the apical region of the PDL. Although some biological studies have empirically analysed fibrous network damage [7,53] and ECM loss [19,54] caused by overstretching of the PDL or interstitial fluid overpressure, our study is the first to provide numerical evidence of these phenomena using a material model that consider fluid and solid phase of the PDL. One unexpected result was the low reaction forces on the cuspid observed in response to parafunctional occlusal forces such as clenching or clenching/grinding. In these scenarios, the posterior teeth supported most of the chewing load, resulting in force reactions of over 300 N, in agreement with previously reported values [24]. Meanwhile, the stress state of the bone adjacent to the cuspid was slightly higher than that observed in normal chewing conditions. Future studies should consider the damage caused to the PDLs of the posterior teeth in these loading conditions. In the grinding condition, the lateral occlusal forces on the cuspid were similar to those observed for traumatic occlusion (around 20 N). Although these loads did not cause damage to the fibrous matrix, there were certain areas in which the hydrostatic pressure of the interstitial fluid was higher than that of capillary blood, indicating the potential for ECM damage. This state of overpressure could account for PDL attachment and bone loss in patients with teeth grinding habits [55].

In summary, in this *in silico* study we evaluated biological damage phenomena in a cuspid PDL under normal, traumatic, and parafunctional 3D loading conditions, using a model that took into account the non-uniform thickness and fluid-fibrous composition of the PDL. Based on our findings we hypothesize that the mechanical stimuli produced during grinding and traumatic occlusion of the cuspid lead to damage of the fibrous network and ECM of the cuspid PDL caused by fibre overstretching and high hydrostatic pressures, respectively. Our data also point to PDL damage in the posterior teeth during clenching as an emerging issue that should be investigated further in future studies.

4.1. Limitations

Our results should be interpreted bearing in mind four main limitations. First, the occlusal loads computed in this study are valid only for the specific patient studied and cannot be directly extrapolated to occlusal models corresponding to other clinical cases. Second, although PDL properties were based on experimental data from animals with chewing systems similar to those of humans, the mechanical properties of the respective

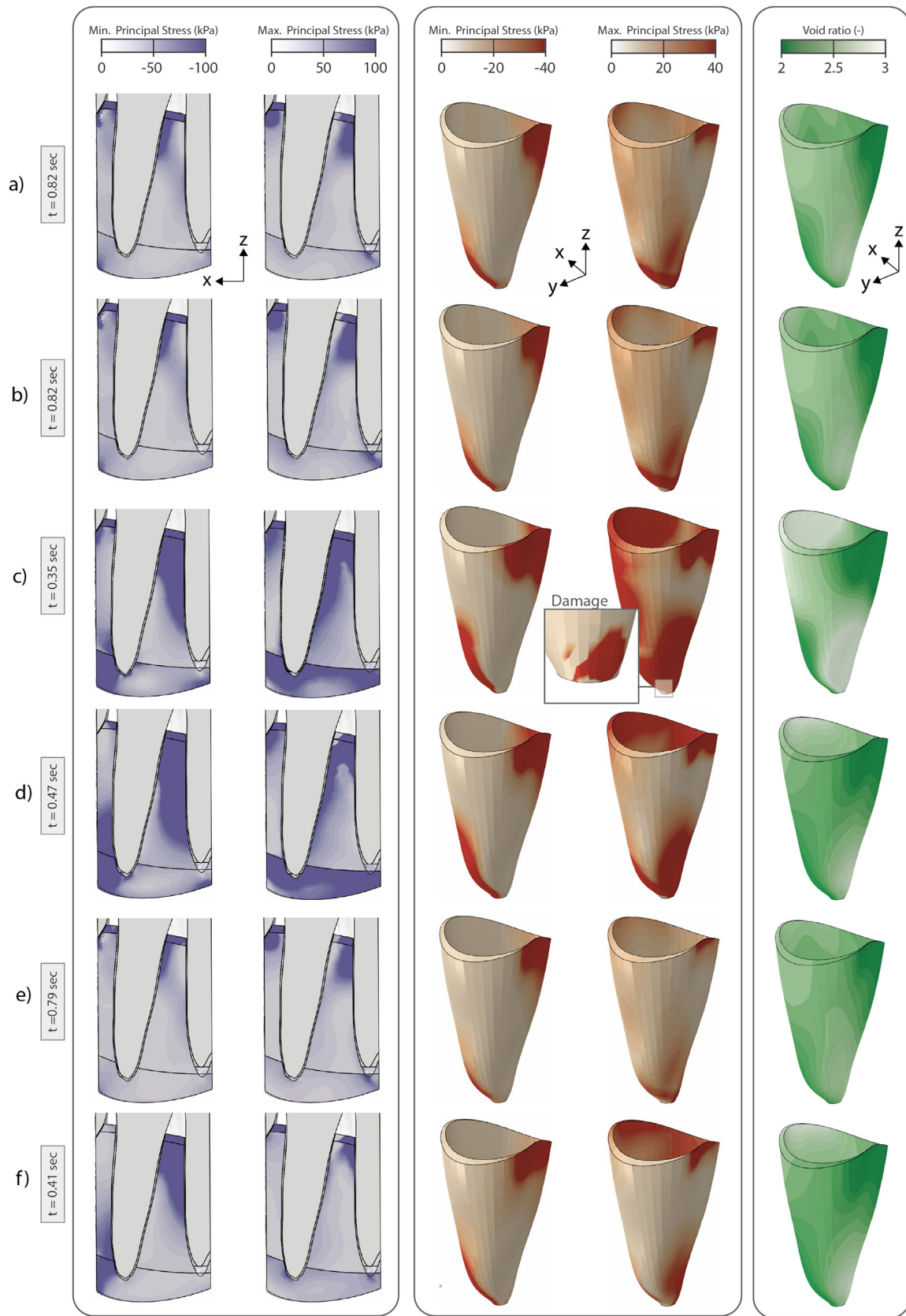**Fig. 6.** Minimum (3rd principal stress) and maximum (1st principal stress) principal stresses in bone regions (first column) and in the PDL of the cuspid tooth (second column) and void ratio in the PDL (third column) at maximum loading time during a) soft chewing; b) hard chewing; c) traumatic cuspid-cuspid occlusion; d) grinding; e) involuntary clenching; and f) combined grinding and clenching.

Fig. 7. Evolution (expressed as percentage of the total duration of the 1st loading-unloading cycle) of the interstitial fluid hydrostatic pressure (left) and of the pressure in the solid matrix (right) under the following load conditions: a) soft chewing; b) hard chewing; c) traumatic cuspid-cuspid occlusion; d) grinding; e) involuntary clenching; and f) combined grinding and clenching. (*Note:* PDL images show axial views).
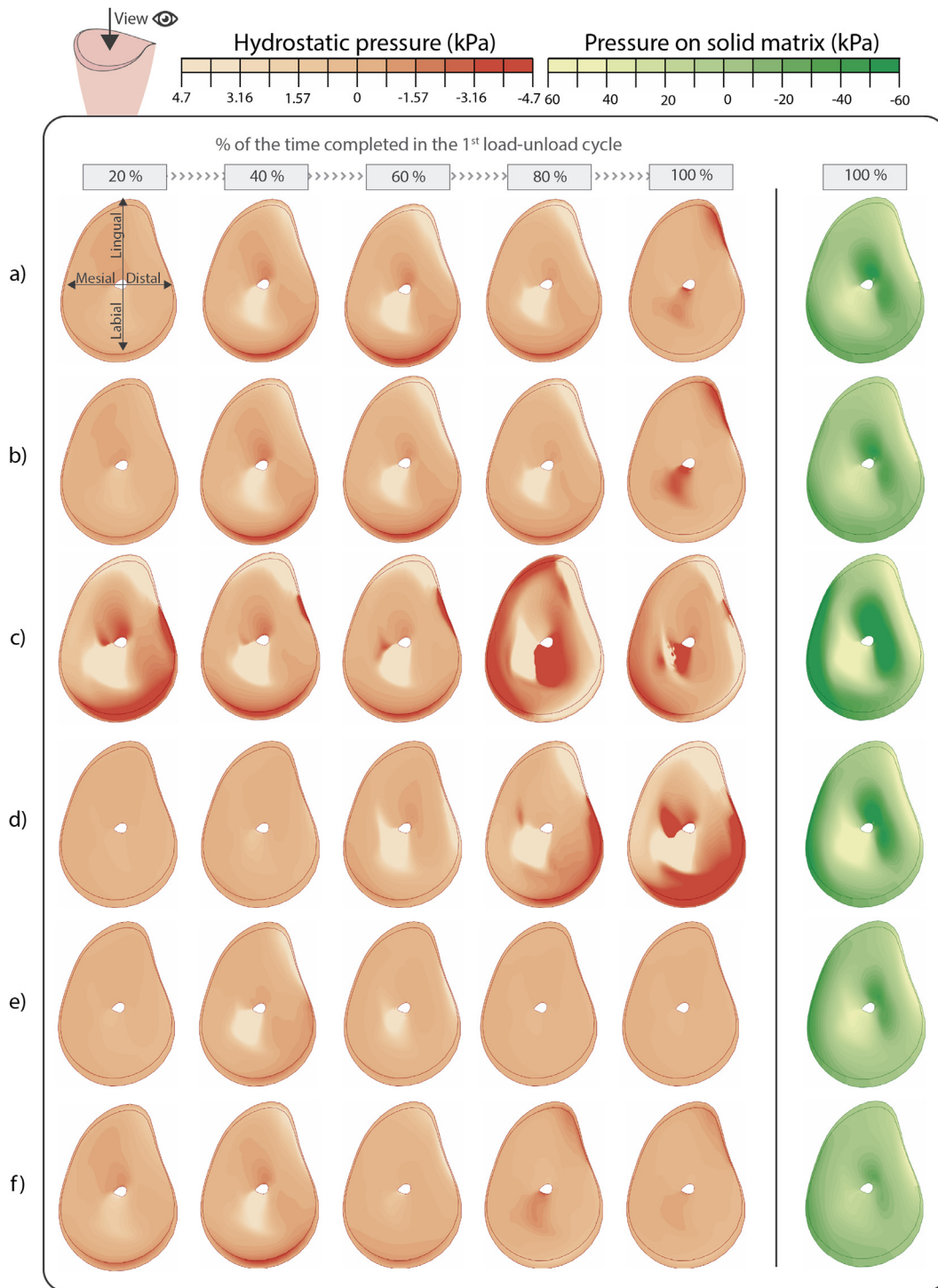
systems may differ. Thirdly, as other studies of the literature [56–58], our model did not allow the condylar translation which is a key factor for the simulation of anteroposterior and medio-lateral movements of the mandible. Finally, owing to the scarcity of data on the magnitude and sequence of muscle forces in deep muscles, we were obliged to estimate the contractile forces for each activity based on the anatomical relationships between muscles.

Bearing these limitations in mind, our results nonetheless could serve to demonstrate a role of the PDL in the origin of oral disorders and serve as a useful basis for the future design and evaluation of dental prostheses and implants. Moreover, our findings highlight several issues that could be addressed in future studies, including the relationship between the mechanobiological responses of the PDL, PDL damage, and the evolution of tooth movement.

5. Conclusion

Within the limitations of this study, we can draw the following conclusions:

1. Early contact of the cuspid tooth could be the main responsible for absorbing lateral occlusal forces, which may serve to validate the basic premise of canine protected occlusion.
2. The response of the PDL to occlusal forces seems to be highly dependent on time and it could be characterised by a persisting stress state between cycles of occlusal forces and residual displacement.
3. In grinding conditions, the PDL of the cuspid tooth seems to be subjected to high lateral compressive loads that could cause ECM damage.
4. Traumatic cuspid-cuspid occlusion could result in deterioration of the fibrous network and the ECM of the PDL which could be caused by fibre overstretching and interstitial fluid overpressure, respectively.

Funding

Declaration of Competing Interest

The authors have no conflicts of interest.

Appendix A. Details of the FE model of the full dentition

The 3D model of the full dentition consisted of a portion of the superior maxilla, the mandible, and the 16 teeth of each arch with their respective periodontal ligaments (PDLs) (Fig. 2a). Hard tissues were segmented by Mimics software (Mimics, v.19.; Materialise, Leuven, Belgium). Firstly, osseous and dental regions of the model were separated through the respective segmentation of the database with threshold levels of 226 HU [1] and 1688 HU [2]. Then, the trabecular bone and the enamel of each tooth were respectively segmented by Mimics default threshold levels of 148 HU and 1553 HU. The results of enamel and trabecular bone segmentation was subtracted from the original segmentation mask to differentiate the cortical and dentin regions. Finally, the pulp of each tooth was defined by the gap inside each tooth.

Mesh

The finite element (FE) mesh was generated using a free meshing technique of 3D solid elements and was refined until further refinement resulted in differences of less than 7%. Except for the PDL, all tissues were meshed using second order tetrahedral elements with mean dimensions of 0.20 mm in all directions and a maximum deviation factor of 0.1. Each PDL was meshed using a second order hexahedral hybrid element along its thickness to avoid excessively increasing the computational cost (Table A.1). Hybrid formulation was required to simulate the incompressible behaviour of the PDL.

Mechanical behaviour of the PDL

The behaviour of the PDL was defined by a nonlinear hyperelastic material model using the fifth order Ogden strain energy function [3], as follows:

$$\psi = \sum_{i=1}^{5} \frac{2\mu_i}{\alpha_i^2} \left(\bar{\lambda}_1^{\alpha_i} + \bar{\lambda}_2^{\alpha_i} + \bar{\lambda}_3^{\alpha_i} - 3 \right) + \sum_{i=1}^{5} \frac{1}{D_i} (J_{el} - 1)^{2i} \qquad (A.1)$$

Table A.1
Types of elements, number of elements, and number of nodes used in each part of the FE model of the full dentition.

FE model of the full dentition			
Region	Element type	No. of elements	No. of nodes
Maxillary cortical bone	C3D10	3,434	15,753
Maxillary trabecular bone	C3D10	67,715	104,042
Mandibular cortical bone	C3D10	28,334	117,933
Mandibular trabecular bone	C3D10	265,566	418,354
PDLs	C3D20H	390,160	2,117,913
Teeth	C3D10	364,970	241,338

where J_{el} is the elastic volume strain, μ and α are material parameters, λ_j is the stretch ratio at principal direction j (related to the strain, ε_j, by $\lambda_i = \varepsilon_j + 1$), and D is related to the bulk modulus. For almost incompressible materials ($D \simeq 0$ and $J_{el} \simeq 1$), the resolution of Eq. (A.1) leads a numerical problem which is solved in Abaqus using hybrid elements formulation. Material parameters were computed by non-linear fitting in MATLAB commercial software (MATLAB 6.0 R12 The MathWorks Inc., Natick, MA, 2000) of the analytical solution (Eq. (A.1)) to experimental compression [4] and stretch [5] data from the literature. Material parameters and the fitted curve for the characterized material model are shown in Table A.2 and Fig. A.1a, respectively.

Modelling of the muscle system

The active (F_a), passive (F_p), and damping (F_d) responses of each chewing muscle were defined through the actuator, spring, and damper components of the connector elements (CONN3D2-type element in Abaqus), respectively. The active force ($F_a = MVC \cdot F_{max}$) of each muscle depended on the activity studied and was determined by multiplying the maximum voluntary clench (MVC) percentage by the maximum force of each muscle (F_{max}) (Table A.3). Due to the lack of available data on the responses of deep muscles, we were obliged to estimate their MVC percentages for each activity based on available values for superficial muscles. For instance, for occlusal trauma the MVC percentages for deep muscles were computed by multiplying MVC values in normal chewing conditions (MVC^{HC}) by c_{OT}, a coefficient of 1.44, which was calculated as the ratio of the MVC percentages for the left superficial masseter in each condition (56.0/38.8). Likewise, the MVC percentages for grinding and involuntary clenching activities were respectively calculated by multiplying by the coefficients c_{Gr} (0.30 [11.6/38.8]) and c_{Cl} (1.72 [67/38.8]). For the grinding condition, only the activity of the muscles of the working side [6] were considered.

Passive muscle stiffness was related to muscle elongation (ε) by $F_p = k\varepsilon/(1 - \varepsilon/a) \cdot PCSA$, where k is the estimated force-length stiffness of the muscles ($k = 40\,N/cm^2$) [7], a is the passive force-length asymptote ($a = 0.7$) [8], and $PCSA$ is the cross-sectional area of the muscle.

Finally, the damping reaction ($F_d = C \cdot \dot{\Delta l}$) was defined as a function of the critical damping coefficient (C) and the stretch velocity in the longitudinal direction, $\dot{\Delta l} = \frac{d(l_F - l_0)}{dt}$ where l_F and l_0 were the instant and initial lengths of the connector respectively. All the parameters for each connector are summarized in Table A.3.

Appendix B. Occlusal analysis by T-scan

The same patient who underwent computed tomography scanning was seated in an upright position to record occlusal contacts using a piezoelectric film sensor. The sensor was inserted into a plastic U-shaped device that was previously selected to match the patient's dentition arch and shape. The U-shaped device was positioned parallel to the upper occlusal plane and was centred along

Table A.2

Mechanical properties assigned to each region of the FE model of the full dentition. E, elastic modulus; v, Poisson coefficient.

Elastic material properties		
Region	E (MPa)	v (−)
Cortical bone	20000[a]	0.30[a]
Dentin	15000[b]	0.31[b]
Enamel	80000[c]	0.31[d]
Pulp	2[e]	0.45[d]
Trabecular bone	345[b]	0.31[b]

Hyperelastic material properties				
PDL	μ_1 (MPa)	μ_2 (MPa)	μ_3 (MPa)	μ_4 (MPa)	μ_5 (MPa)

μ_1 (MPa)	μ_2 (MPa)	μ_3 (MPa)	μ_4 (MPa)	μ_5 (MPa)
−3420.83	1434.35	−5.56E−04	3345.65	−1365.88
α_1 (−)	α_2 (−)	α_3 (−)	α_4 (−)	α_5 (−)
−0.506	−0.134	13.708	−1.029	−1.397
D_1 (MPa^{-1})	D_2 (MPa^{-1})	D_3 (MPa^{-1})	D_4 (MPa^{-1})	D_5 (MPa^{-1})
0	0	0	0	0

[a] Lacroix and Prendergast, 2002 [9].
[b] Bergomi et al., 2011 [4].
[c] Nikolaus et al., 2016 [10].
[d] Belli et al., 2017 [11].
[e] Lin et al., 2014 [12].
[f] Ortún-Terrazas et al., 2018 [13].
[g] Ortún-Terrazas et al., 2019 [14].

Table A.3

Parameters used to compute F_a, F_p, and F_d values for each muscle on the right (R) and left (L) sides during hard (HC) and soft (SC) chewing, occlusal trauma (OT), grinding (Gr), and involuntary clenching (Cl). SM, superficial masseter; AT, anterior temporalis; DM, deep masseter; PT, posterior temporalis; IHLP, inferior head of lateral pterygoid; MP, medial pterygoid; R, right side; L, left side.

Muscle ID	F_{max}(N)	PCSA (cm^2)	C (N/μm)	Side	L_0(mm)	MVC (%)				
						HC	SC	OT	Gr	Cl
SM	272.8[a]	4.76[b]	0.053[c]	L	52.8	38.8[d]	35.9[d]	56.0[e]	11.6[d]	67.0[f]
				R	54.5	31.6[d]	20.3[d]	46.8[e]	6.9[d]	66.0[f]
AT	308.0[a]	3.95[b]	0.035[c]	L	57.9	34.5[d]	29.4[d]	46.3[e]	12.9[d]	84.0[f]
				R	74.1	25.2[d]	22.5[d]	32.2[e]	8.3[d]	83.0[f]
DM	73.8[a]	2.04[b]	0.038[c]	L	55.0	23.4[g]	33.8[h]	7.0[i]	40.5[j]
				R	74.1	12.9[g]	18.6[h]	–	22.2[j]
PT	222.0[a]	1.89[b]	0.023[c]	L	70.1	8.4[g]	12.1[h]	2.5[i]	14.5[j]
				R	85.8	9.7[g]	14.0[h]	–	16.8[j]
ILP	112.8[a]	1.67[b]	0.021[c]	L	32.0	1.9[g]	2.7[h]	–	3.2[j]
				R	46.0	1.9[g]	2.8[h]	0.6[i]	3.4[j]
MP	240[a]	4.37[b]	0.060[c]	L	46.3	11.8[g]	17.1[h]	–	20.4[j]
				R	47.8	13.5[g]	19.5[h]	4.1[i]	23.4[j]

[a] Koolstra and van Eijden [15].
[b] Peck et al. [7].
[c] Langenbach and Hannam [16].
[d] Farella et al. [17].
[e] Pérez del Palomar et al. [18].
[f] Cecílio et al. [19].
[g] Computed based on the muscles forces reported by Langenbach and Hannam [16] and the F_{max} of the muscle.
[h] Computed using $MVC^{HC} \bullet c_{OT}$.
[i] Computed using $MVC^{HC} \bullet c_{Gr}$.
[j] Computed using $MVC^{HC} \bullet c_{Cl}$.

the midline between the central incisor teeth by a dentist with expertise in the occlusal analysis. The film consisted of a 100-µm-thick mylar-encased recording sensor with 1500 compressible sensitive receptor points. The sensitivity range of the film was established before recording.

The patient was instructed to chew the pressure-sensitive film, applying maximum voluntary force. The analysis was repeated 3 times and the analysis with the most balanced occlusion (Fig. 3b) was selected for comparison with the occlusal contacts produced by the FE model (Fig. 3a). The patient was also instructed to grind their teeth to record the relative percentage of the total bite force, and its distribution across both halves of the dentition (Fig. 3c).

The contact pressures in our simulations were recorded using a virtual square-shape film with a thickness of 0.1 mm. The virtual film body was manually centred along the central incisor teeth

midpoint. The film was composed of 11,200 s-order quadrilateral membrane elements (M3D8-type element in Abaqus) and its behaviour was defined based on the linear elastic properties of Mylar840 (DuPont; $E = 5$ GPa and $v = 0.3$). To plot the contact results shown in Fig. 3a, the contact reaction forces of the centroid node of each element were extracted using a Python script ("Python 3.5.2, Python Software Foundation") and the values plotted on a 3D bars graph in MATLAB.

Appendix C. Details of the single tooth FE model

A portion of a human mandible was extracted from a cadaver within 4 h after death and stored frozen (−20 °C) until it was scanned. Prior to scanning, the sample was taken from the freezer and allowed to thaw at room temperature (17 °C). The soft tissues attached to the mandible were carefully removed and the cleaned
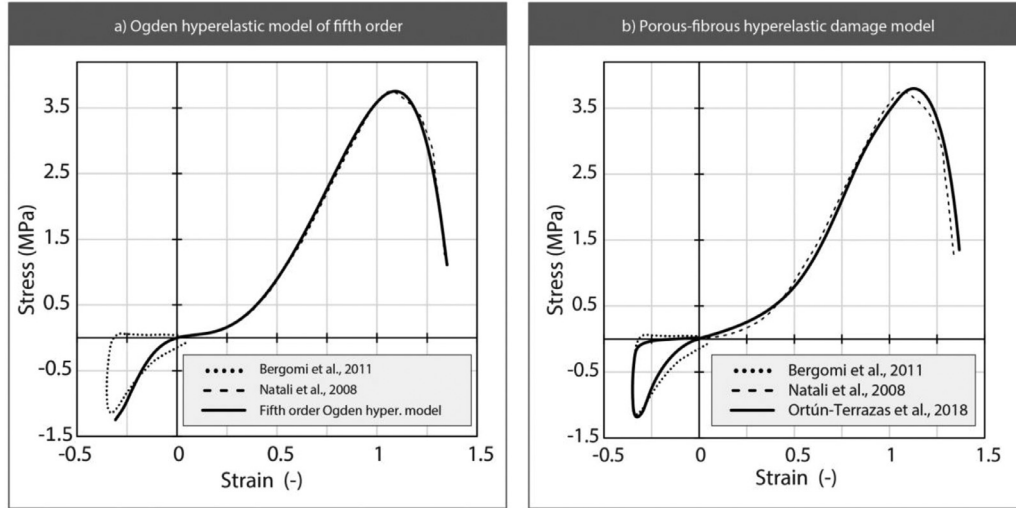
Fig. A.1. Fitted curve obtained by approximation to the experimental data published by Natali et al. (2008) and Bergomi et al. (2011) using a) fifth order Ogden hyperelastic model and b) a porous-fibrous hyperelastic damage model previously characterized by our group [14].

specimen was scanned by μCT scan (Skyscan 1172, Bruker μCT N.V., Kontich, Bélgica). μCT data was collected using 13-μm cross-sections to ensure resolution. Next, the tomographic images generated after scanning were rebuilt, the noise was reduced, and the point cloud was converted into Non-Uniform Rational Bases Splines (NURBS) using Rhinoceros software (Rhinoceros v.5, Robert McNeel & Associates, Seattle, USA). Because PDLs could not be detected by μCT, they were defined within the free space between the trabecular bone and the teeth. The model was composed of an entire cuspid tooth and 2 partial teeth (a premolar and a lateral incisal) with their respective PDLs embedded in the mandibular bone (Fig. 2b). Further information on the development of this model is provided in a previous publication by our group [13].

Mesh

Mesh refinement was performed until further refinement resulted in differences of 5% or less. The PDL of the cuspid tooth was meshed throughout its thickness using 3 first-order hexahedral elements. The other 2 PDLs were meshed along their thickness using a quadratic element; while the incomplete shape of these ligaments complicated the mesh refinement process, the data obtained from these ligaments were not the main goal of this study. Regardless, the effect of the mesh size on these PDLs was negligible given the low stress/strain values to which they were subjected. The remaining regions were meshed by tetrahedral linear elements with mean dimensions of 0.2 mm in all directions and a maximum deviation factor of 0.15. Further information on the meshing process is provided in Table C.1.

Mechanical behaviour of the PDL

According to previous findings [5,13,14,20,21], the PDL undergoes 2 types of softening phenomena caused by fibre uncrimping and rupture, and displays 2 different behaviours owing to its porous-fibrous structure. Therefore, energy density function (ψ) of the porous transversely-isotropic-hyperelastic-damage material model was formulated as follows:

$$\psi = \eta \cdot \left[\psi_m(\tilde{I}_1) + (1 - D_f) \cdot \psi_f(\tilde{I}_4) \right] + \Phi(\eta) + \psi_{vol}(J_{el}) \qquad (C.1)$$

Where ψ_m and ψ_f are the ground matrix and fibrous terms of the deviatoric component (ψ_{dev}), $D_f \in [0,1]$ is the damage parameter

Table C.1
Types of elements, number of elements, and number of nodes used in each region of the FE model of a single tooth.

FE model of the single tooth			
Region	Element type	No. elements	No. nodes
Cortical bone	C3D4	4,118	2,315
Cuspid tooth	C3D4P	48,499	27,267
Cuspid PDL	C3D8RP	40,716	22,892
Lateral incisor PDL	C3D20	3,157	1,776
Lateral incisor tooth	C3D4P	52,547	29,543
Premolar PDL	C3D20	3,360	1,889
Premolar tooth	C3D4P	52,819	29,696
Trabecular bone	C3D4P	62,697	35,250

that explains the evolution of damage due to fibre rupture, Φ is the energy dissipated, ψ_{vol} is the volumetric term and η is the damage variable for softening due to fibre uncrimping which varies with deformation, as follows:

$$\eta = 1 - \frac{1}{r} errf\left(\frac{\psi_{dev}^m - \psi_{dev}}{m + \beta_m \psi_{dev}^m} \right) \qquad (C.2)$$

where r and β_m are dimensionless material parameters, m is a parameter with the dimensions of energy, ψ_{dev}^m is the maximum value of the deviatoric strain energy density experienced by the material during its deformation history, and $errf$ is the error function defined by $errf(x) = \frac{2}{\sqrt{\pi}} \int_0^x \exp(-\omega^2)d\omega$.

The energy dissipation term Φ was defined by the Ogden-Roxburgh model as follows:

$$\Phi(\eta) = \frac{(m + \beta_m \psi_{dev}^m)}{r\sqrt{\pi}} \left\{ \exp\left[-\left(\frac{\psi_{dev}^m - \psi_{dev}}{m + \beta_m \psi_{dev}^m} \right) \right]^2 - 1 \right\} + (1 - \eta)\psi_{dev}^m \qquad (C.3)$$

To consider porous-fibrous different contributions, the terms ψ_{dev} and ψ_{vol} were described by 2 different material models according to the direction of fibre stretch. Therefore, ψ_{dev} and ψ_{vol} are described by a porous hyperfoam material formulation [22] when PDL was compressed ($\tilde{I}_4 \leq 1$), and by a porous transversely isotropic hyperelastic damage material model [23] when the tissue is stretched ($\tilde{I}_4 > 1$).

The dilatational ($\tilde{I}_1$) and deviatoric ($\tilde{I}_4$) invariants are defined as follows:

$$\tilde{I}_1 = tr\tilde{\boldsymbol{C}}; \quad \tilde{I}_4 = \boldsymbol{a}^0 \cdot \tilde{\boldsymbol{C}} \cdot \boldsymbol{a}^0 \tag{C.4}$$

where $\boldsymbol{a}^0$ is a unitary vector defining the orientation of the collagen fibres and $\tilde{\boldsymbol{C}}$ is the modified Green tensor in the reference configuration, defined by the deformation gradient $\tilde{\boldsymbol{F}}$, as $\tilde{\boldsymbol{C}}(\hat{\lambda}_i) = \tilde{\boldsymbol{F}}^T\tilde{\boldsymbol{F}}$. The stretch ($\hat{\lambda}_i$) is determined as the ratio between fibre lengths in deformed ($\boldsymbol{X}$) and reference ($\boldsymbol{x}$) configurations in direction i. The deformation gradient is therefore expressed by the Jacobian elastic tensor as $\tilde{\boldsymbol{F}} = J_{el}^{-\frac{1}{3}}\boldsymbol{F}$. The terms ψ_{vol} and ψ_{dev} of the energy density function are written as follows:

$$\psi_{vol} = \begin{cases} \frac{1}{\beta}\left[(J_{el})^{-\alpha\beta} - 1\right] & if \ (\tilde{I}_4 < 1) & \text{(C.5)} \\ \frac{1}{D}\left[\frac{(J_{el})^2-1}{2} - \ln J_{el}\right] & if \ (\tilde{I}_4 \geq 1) & \text{(C.6)} \end{cases}$$

$$\psi_{dev} = \begin{cases} \frac{2\mu}{\alpha^2}\left[\hat{\lambda}_1^\alpha + \hat{\lambda}_2^\alpha + \hat{\lambda}_3^\alpha\right] & if \ (\tilde{I}_4 < 1) & \text{(C.7)} \\ C_1 \cdot (\tilde{I}_1 - 3) + (1 - D_f) \cdot \frac{k_1}{2 \cdot k_2}\left\{exp\left[k_2 \cdot (\tilde{I}_4 - 1)^2\right] - 1\right\} & if \ (\tilde{I}_4 \geq 1) & \text{(C.8)} \end{cases}$$

In Eq. C.5, α is a dimensionless material parameter of the porous hyperfoam material, and β determines the degree of compressibility related to the Poisson ratio by $\beta = \nu/(1 - 2\nu)$. The parameter D of Eq. C.6 is related to the bulk modulus, K, by $K = 2/D$.

μ and α are material parameters of the deviatoric term of the hyperfoam material model (Eq. C.7). In Eq. C.8, C_1 is a material constant related to the ground substance of the transversely isotropic material model, $k_1 > 0$ and $k_2 > 0$ are the parameters that identify the exponential behaviour due to the presence of the collagen fibres, and the damage parameter, D_f, explains the evolution of damage due to fibre rupture as follows:

$$D_f(\Xi_t^m) = \frac{1}{2}\left\{1 + \frac{\alpha_f \Xi_t^m e^{2\alpha_f\left[(2\Xi_t^m/\beta_f)-1\right]} - 1}{\alpha_f \Xi_t^m e^{2\alpha_f\left[(2\Xi_t^m/\beta_f)-1\right]} + 1}\right\} \tag{C.9}$$

where α_f and β_f are 2 material parameters and Ξ_t^m is the maximum value of Ξ_s over past history up to the current time s. Ξ_s is the equivalent strain [24] at any time s defined by $\Xi_s(\tilde{\boldsymbol{C}}) = \sqrt{2 \cdot \psi_f(\tilde{I}_4) \cdot \tilde{\boldsymbol{C}}(s)}$ where the fibrous term ψ_f corresponds to the second term of Eq. C.8.

To account for the biphasic behaviour of the PDL a porous contribution was added to the model. In the fully saturated tissue, total stress at a given point $\boldsymbol{\sigma}$ is defined [25] as follows:

$$\boldsymbol{\sigma} = (1 - e) \cdot \bar{\boldsymbol{\sigma}} - e \cdot \bar{p}_t \cdot \boldsymbol{I} - \zeta \cdot \bar{p}_t \cdot \boldsymbol{I} \tag{C.10}$$

where e is the void ratio related to the porosity of a tissue (n) by $e = n/(1 - n)$, being n defined by the volume of the fluid phase V_f in the total volume of the tissue V_t, ζ is a factor that depends on

Table C.2
Mechanical properties assigned to each region of the FE model of a single tooth. E, elastic modulus; ν, Poisson coefficient; Υ_w, specific weight of interstitial fluid.

Elastic material model

Region	E (MPa)	$\nu\ (-)$
Pulp[a]	3	0.45
Enamel[b]	80000	0.31
Cortical bone[c]	20000	0.30

Porous elastic material model

Region	E (MPa)	$\nu\ (-)$	$k_0 \cdot 10^{-15}\ (m^2)$	$M\ (-)$	$e_0(-)$	$\Upsilon_w \cdot 10^{-6}\ (N/mm^3)$
Trabecular bone[d]	345	0.31	52.9	–	4	9.8
Dentin[d]	15000	0.31	0.038	–	4	9.8

Transversally isotropic material model

Region	$C_1(MPa)$	$D(MPa^{-1})$	$k_1(MPa)$	$k_2\ (-)$
Premolar PDL[e]	0.01	9.078	0.298	1.525
Incisor PDL[e]	0.01	9.078	0.298	1.525

Porous transversally isotropic material model

Region	$C_1(MPa)$	$D(MPa^{-1})$	$k_1(MPa)$	$k_2(-)$	$k_0 \cdot 10^{-15}(m^2)$	$M\ (-)$	$e_0(-)$	$\Upsilon_w \cdot 10^{-6}\ (N/mm^3)$
Cuspid PDL ($\tilde{I}_4 \geq 1$)	0.01[e]	9.078[e]	0.298[e]	1.525[e]	6.5[e]	9.5[e]	2.33[d]	9.8

Porous hyperfoam material model

Region	$\mu\ (MPa)$	$\alpha\ (-)$	$\nu\ (-)$	$k_0 \cdot 10^{-15}(m^2)$	$M\ (-)$	$e_0(-)$	$\Upsilon_w \cdot 10^{-6}(N/mm^3)$
Cuspid PDL ($\tilde{I}_4 < 1$)[d]	0.03	20.9	0.257	8.81	14.2	2.33	9.8

Fibre uncrimping

Region	$r\ (-)$	$m\ (mJ)$	$\beta_m\ (-)$
Cuspid PDL[g]	1.492	0.064	0.1

Fibres rupture

Region	$\alpha_f\ (-)$	$\beta_f\ (-)$	$\Xi_s^{max}\ (-)$
Cuspid PDL[g]	1.0	0.25	0.28

[a] Belli et al., 2017 [11].
[b] Nikolaus et al., 2016 [10].
[c] Lacroix and Prendergast, 2002 [9].
[d] Bergomi et al., 2011 [4].
[e] Ortún-Terrazas et al., 2018 [13].
[g] Ortún-Terrazas et al., 2019 [14].
[h] Wei et al. 2014 [28].

saturation, $\bar{\sigma}$ is the effective stress of the solid matrix, and $\bar{p}_t$ is the average pressure stress related to tissue permeability by the non-linear Forchheimer flow law and implemented in Abaqus. To relate permeability to deformation, the exponential function described by Argoubi and Shirazi-Adl [26] was used as follows:

$$\bar{k} = k_0 \left[\frac{e(1+e_0)}{e_0(1+e)} \right]^2 exp\left[M\left(\frac{1+e}{1+e_0} - 1 \right) \right] \tag{C.11}$$

where k_0 and e_0 are the permeability and void ratio at zero strain, and M is a dimensionless material parameter.

The damage parameters m, r and β_m of Eq. (C.2) were defined based on the experimental data of Natali et al. [27]. Material parameters C_1, k_1, k_2, D, α_f and β_f were defined based on later experimental data published by Natali et al. [5]. Finally, parameters μ, α, β, and M were defined based on experimental compression test data from Bergomi et al. [4]. The material formulation and the characterization of aforementioned parameters have been fully described in our previous publications [13,14]. The material parameters and the material response mimicked are shown in Table C.2 and Fig. A.1b, respectively.

Appendixes references

[1] H. Lin, P. Zhu, Y. Lin, S. Wan, X. Shu, Y. Xu, Y. Zheng, Mandibular asymmetry: A three-dimensional quantification of bilateral condyles, Head Face Med. 9 (2013) 1–7. doi:10.1186/1746–160x-9–42.

[2] Y. Wang, S. He, L. Yu, J. Li, S. Chen, Accuracy of volumetric measurement of teeth *in vivo* based on cone beam computer tomography, Orthod. Craniofac. Res. 14 (2011) 206–212. doi:10.1111/j.1601–6343.2011.01525.x.

[3] R.W. Ogden, Non linear elastic deformations, 1997.

[4] M. Bergomi, J. Cugnoni, M. Galli, J. Botsis, U.C. Belser, H.W.A. Wiskott, Hydro-mechanical coupling in the periodontal ligament: A porohyperelastic finite element model, J. Biomech. 44 (2011) 34–38. doi:10.1016/j.jbiomech.2010.08.019.

[5] A.N. Natali, E.L. Carniel, P.G. Pavan, F.G. Sander, C. Dorow, M. Geiger, A visco-hyperelastic-damage constitutive model for the analysis of the biomechanical response of the periodontal ligament., J. Biomech. Eng. 130 (2008) 31004. doi:10.1115/1.2900415.

[6] A.J. Miller, Craniomandibular muscles: Their role in function and form, CRC Press, 2017. doi:10.4324/9781315150550.

[7] C.C. Peck, G.E.J. Langenbach, A.G. Hannam, Dynamic simulation of muscle and articular properties during human wide jaw opening, Arch. Oral Biol. 45 (2000) 963–982. doi:10.1016/S0003–9969(00)00071–6.

[8] van der M.J. Horst, Human Head Neck Response in Frontal, Lateral and Rear End Impact Loading - modelling and validation -, 2002. doi:10.6100/IR554047.

[9] D. Lacroix, P.J. Prendergast, A mechano-regulation model for tissue differentiation during fracture healing: analysis of gap size and loading, J. Biomech. 35 (2002) 1163–1171. doi:10.1016/S0021–9290(02)00086–6.

[10] A. Nikolaus, C. Fleck, T. Lindtner, J. Currey, P. Zaslansky, Importance of the variable periodontal ligament geometry for whole tooth mechanical function: A validated numerical study, J. Mech. Behav. Biomed. Mater. 67 (2016) 61–73. doi:10.1016/j.jmbbm.2016.11.020.

[11] S. Belli, O. Eraslan, G. Eskitaşcioğlu, Effect of Different Treatment Options on Biomechanics of Immature Teeth: A Finite Element Stress Analysis Study, J. Endod. (2017). doi:10.1016/j.joen.2017.08.037.

[12] S.-L. Lin, S.-Y. Lee, Y.-C. Lin, Y.-H. Huang, J.-C. Yang, H.-M. Huang, Evaluation of mechanical and histological properties of cryopreserved human premolars under short-term preser-vation: A preliminary study, J. Dent. Sci. 9 (2014) 244–248. doi:10.1016/j.jds.2013.04.010.

[13] J. Ortún-Terrazas, J. Cegoñino, U. Santana-Penín, U. Santana-Mora, A. Pérez del Palomar, Approach towards the porous fibrous structure of the periodontal ligament using micro-computerized tomography and finite element analysis, J. Mech. Behav. Biomed. Mater. 79 (2018) 135–149. doi:10.1016/j.jmbbm.2017.12.022.

[14] J. Ortún-Terrazas, J. Cegoñino, U. Santana-Penín, U. Santana-Mora, A. Pérez del Palomar, A porous fibrous hyperelastic damage model for human periodontal ligament: Application of a micro-computerized tomography finite element model., Int. j. Numer. Method. Biomed. Eng. (2019) e3176. doi:10.1002/cnm.3176.

[15] J.H.H. Koolstra, T.M.G.J.M.G.J. van Eijden, Combined finite-element and rigid-body analysis of human jaw joint dynamics, J. Biomech. 38 (2005) 2431–2439. doi:10.1016/j.jbiomech.2004.10.014.

[16] G.E.J. Langenbach, A.G. Hannam, The role of passive muscle tensions in a three-dimensional dynamic model of the human jaw, Arch. Oral Biol. 44 (1999) 557–573. doi:10.1016/S0003–9969(99)00034–5.

[17] M. Farella, S. Palla, S. Erni, A. Michelotti, L.M. Gallo, Masticatory muscle activity during deliberately performed oral tasks, Physiol. Meas. 29 (2008) 1397–1410. doi:10.1088/0967–3334/29/12/004.

[18] A. Pérez del Palomar, U. Santana-Penín, M.J. Mora-Bermúdez, M. Doblaré, Clenching TMJs-Loads Increases in Partial Edentates: A 3D Finite Element Study, Ann. Biomed. Eng. 36 (2008) 1014–1023. doi:10.1007/s10439-008–9487-y.

[19] F.A. Cecílio, S.C.H.H. Regalo, M. Palinkas, J.P.M.M. Issa, S. Siéssere, J.E.C.C. Hallak, J.P. Machado-de-sousa, M. Semprini, Ageing and surface EMG activity patterns of masticatory muscles, J. Oral Rehabil. 37 (2010) 248–255. doi:10.1111/j.1365–2842.2010.02051.x.

[20] M. Bergomi, H.W.A. Wiskott, J. Botsis, A. Mellal, U.C. Belser, Load Response of Periodontal Ligament: Assessment of Fluid Flow, Compressibility, and Effect of Pore Pressure, J. Biomech. Eng. 132 (2009) 014504. doi:10.1115/1.4000154.

[21] A.N. Natali, P.G. Pavan, E.L. Carniel, C. Dorow, A Transversally Isotropic Elasto-damage Constitutive Model for the Periodontal Ligament, Comput. Methods Biomech. Biomed. Engin. 6 (2003) 329–336. doi:10.1080/10255840310001639840.

[22] B. Storakers, On material representation and constitutive branching in finite compressible elasticity, J. Mech. Phys. Solids. 34 (1986) 125–145. doi:10.1016/0022–5096(86)90033–5.

[23] J.F. Rodríguez, F. Cacho, J.A. Bea, M. Doblaré, A stochastic-structurally based three dimensional finite-strain damage model for fibrous soft tissue, J. Mech. Phys. Solids. 54 (2006) 864–886. doi:10.1016/j.jmps.2005.10.005.

[24] E. Peña, B. Calvo, M.A. Martínez, M. Doblaré, On finite-strain damage of viscoelastic-fibred materials. Application to soft biological tissues, Int. J. Numer. Methods Eng. 74 (2008) 1198–1218. doi:10.1002/nme.2212.

[25] T.H. Wu, Soil mechanics, (1967).

[26] M. Argoubi, A. Shirazi-Adl, Poroelastic creep response analysis of a lumbar motion segment in compression, J. Biomech. 29 (1996) 1331–1339. doi:10.1016/0021–9290(96)00035–8.

[27] A.N. Natali, P.G. Pavan, E.L. Carniel, C. Dorow, Viscoelastic response of the periodontal ligament: An experimental-numerical analysis, Connect. Tissue Res. 45 (2004) 222–230. doi:10.1080/03008200490885742.

[28] Z. Wei, X. Yu, X. Xu, X. Chen, Experiment and hydro-mechanical coupling simulation study on the human periodontal ligament, Comput. Methods Programs Biomed. 113 (2014) 749–756. doi:10.1016/j.cmpb.2013.12.011.

References

[1] C.C. Peck, A.G. Hannam, Human jaw and muscle modelling, Arch. Oral Biol. 52 (2007) 300–304, doi:10.1016/j.archoralbio.2006.11.004.

[2] J.P. Hatch, R.S.A. Shinkai, S. Sakai, J.D. Rugh, E.D. Paunovich, Determinants of masticatory performance in dentate adults, Arch. Oral Biol. 46 (2001) 641–648.

[3] W.H. Organization, Oral Health Surveys: Basic Methods, World Health Organization, 2013.

[4] A.N. Natali, P.G. Pavan, C. Scarpa, Numerical analysis of tooth mobility: formulation of a non-linear constitutive law for the periodontal ligament, Dent. Mater. 20 (2004) 623–629, doi:10.1016/j.dental.2003.08.003.

[5] C.G. Provatidis, A comparative FEM-study of tooth mobility using isotropic and anisotropic models of the periodontal ligament, Med. Eng. Phys. 22 (2000) 359–370, doi:10.1016/S1350-4533(00)00055-2.

[6] K. Reitan, The initial tissue reaction incident to orthodontic tooth movement as related to the influence of function, Acta Odonto. Scand. 6 (1951) 1–240.

[7] S. Nakatsu, Y. Yoshinaga, A. Kuramoto, F. Nagano, I. Ichimura, K. Oshino, A. Yoshimura, Y. Yano, Y. Hara, Occlusal trauma accelerates attachment loss at the onset of experimental periodontitis in rats, J. Periodontal Res. 49 (2014) 314–322, doi:10.1111/jre.12109.

[8] I.Z. Oskui, A. Hashemi, H. Jafarzadeh, Biomechanical behavior of bovine periodontal ligament: experimental tests and constitutive model, J. Mech. Behav. Biomed. Mater. 62 (2016) 599–606, doi:10.1016/j.jmbbm.2016.05.036.

[9] A.N. Natali, P.G. Pavan, E.L. Carniel, C. Dorow, A transversally isotropic elasto-damage constitutive model for the periodontal ligament, Comput. Methods Biomech. Biomed. Engin. 6 (2003) 329–336, doi:10.1080/10255840310001639840.

[10] A.N. Natali, E.L. Carniel, P.G. Pavan, F.G. Sander, C. Dorow, M. Geiger, A visco-hyperelastic-damage constitutive model for the analysis of the biomechanical response of the periodontal ligament., J. Biomech. Eng. 130 (2008) 31004, doi:10.1115/1.2900415.

[11] F. Genna, L. Annovazzi, C. Bonesi, P. Fogazzi, C. Paganelli, On the experimental determination of some mechanical properties of porcine periodontal ligament, Meccanica 43 (2008) 55–73, doi:10.1007/s11012-007-9094-2.

[12] T. Tsuzuki, H. Kajiya, K. T-Goto, T. Tsutsumi, T. Nemoto, K. Okabe, Y. Takahashi, Hyperocclusion stimulates the expression of collagen type XII in periodontal ligament, Arch. Oral Biol. 66 (2016) 86–91, doi:10.1016/j.archoralbio.2016.02.009.

[13] Y. Ujiie, A. Shimada, K. Komatsu, S. Gomi, S. Oida, T. Arai, M. Fukae, Degradation of noncollagenous components by neutrophil elastase reduces the mechanical strength of rat periodontal ligament, J. Periodontal Res. (2007) 070508213437001–???, doi:10.1111/j.1600-0765.2007.00990.x.

[14] B.K.B. Berkovitz, G.R. Holland, B.J. Moxham, Oral Anatomy, Histology and Embryology E-Book, Elsevier Health Sciences, 2017.

[15] M. Bergomi, J. Cugnoni, M. Galli, J. Botsis, U.C. Belser, H.W.A. Wiskott, Hydromechanical coupling in the periodontal ligament: a porohyperelastic finite element model, J. Biomech. 44 (2011) 34–38, doi:10.1016/j.jbiomech.2010.08.019.

[16] J. Ortún-Terrazas, J. Cegoñino, U. Santana-Penín, U. Santana-Mora, A. Pérez del Palomar, Approach towards the porous fibrous structure of the periodontal ligament using micro-computerized tomography and finite element analysis, J. Mech. Behav. Biomed. Mater. 79 (2018) 135–149, doi:10.1016/j.jmbbm.2017.12.022.

[17] Z. Wei, X. Yu, X. Xu, X. Chen, Experiment and hydro-mechanical coupling simulation study on the human periodontal ligament, Comput. Methods Programs Biomed. 113 (2014) 749–756, doi:10.1016/j.cmpb.2013.12.011.

[18] M. Bergomi, H.W.A. Wiskott, J. Botsis, A. Mellal, U.C. Belser, Load response of periodontal ligament: assessment of fluid flow, compressibility, and effect of pore pressure, J. Biomech. Eng. 132 (2009) 014504, doi:10.1115/1.4000154.

[19] J. Chen, W. Li, M.V. Swain, M. Ali Darendeliler, Q. Li, M.A. Darendeliler, Q. Li, A periodontal ligament driven remodeling algorithm for orthodontic tooth movement, J. Biomech. 47 (2014) 1689–1695, doi:10.1016/j.jbiomech.2014.02.030.

[20] M. Pini, P. Zysset, J. Botsis, R. Contro, Tensile and compressive behaviour of the bovine periodontal ligament, J. Biomech. 37 (2004) 111–119, doi:10.1016/S0021-9290(03)00234-3.

[21] J. Ortún-Terrazas, J. Cegoñino, U. Santana-Penín, U. Santana-Mora, A. Pérez del Palomar, A porous fibrous hyperelastic damage model for human periodontal ligament: application of a micro-computerized tomography finite element model, Int. J. Numer. Method. Biomed. Eng. (2019) e3176, doi:10.1002/cnm.3176.

[22] R.Y. Dhume, E.D. Shih, V.H. Barocas, Multiscale model of fatigue of collagen gels, Biomech. Model. Mechanobiol. 18 (2019) 175–187, doi:10.1007/s10237-018-1075-y.

[23] T.S. Fill, J.P. Carey, R.W. Toogood, P.W. Major, Experimentally determined mechanical properties of, and models for, the periodontal ligament: critical review of current literature, J. Dent. Biomech. 2 (2011) 312980–312980, doi:10.4061/2011/312980.

[24] O. Röhrle, H. Saini, D.C. Ackland, Occlusal loading during biting from an experimental and simulation point of view, Dent. Mater. 34 (2018) 58–68, doi:10.1016/j.dental.2017.09.005.

[25] S. Benazzi, H.N. Nguyen, O. Kullmer, K. Kupczik, Dynamic modelling of tooth deformation using occlusal kinematics and finite element analysis, PLoS ONE 11 (2016) 1–17, doi:10.1371/journal.pone.0152663.

[26] A. Nikolaus, C. Fleck, T. Lindtner, J. Currey, P. Zaslansky, Importance of the variable periodontal ligament geometry for whole tooth mechanical function: a validated numerical study, J. Mech. Behav. Biomed. Mater. 67 (2016) 61–73, doi:10.1016/j.jmbbm.2016.11.020.

[27] G.R.S. Naveh, V. Brumfeld, R. Shahar, S. Weiner, Tooth periodontal ligament: direct 3D microCT visualization of the collagen network and how the network changes when the tooth is loaded, J. Struct. Biol. 181 (2013) 108–115, doi:10.1016/j.jsb.2012.10.008.

[28] A.N. Natali, P.G. Pavan, C. Venturato, K. Komatsu, Constitutive modeling of the non-linear visco-elasticity of the periodontal ligament, Comput. Methods Programs Biomed. 104 (2011) 193–198, doi:10.1016/j.cmpb.2011.03.014.

[29] H. Huang, W. Tang, Q. Tan, B. Yan, Development and parameter identification of a visco-hyperelastic model for the periodontal ligament, J. Mech. Behav. Biomed. Mater. 68 (2017) 210–215, doi:10.1016/j.jmbbm.2017.01.035.

[30] H. Lin, P. Zhu, Y. Lin, S. Wan, X. Shu, Y. Xu, Y. Zheng, Mandibular asymmetry: a three-dimensional quantification of bilateral condyles, Head Face Med. 9 (2013) 1–7, doi:10.1186/1746-160x-9-42.

[31] Y. Wang, S. He, L. Yu, J. Li, S. Chen, Accuracy of volumetric measurement of teeth in vivo based on cone beam computer tomography, Orthod. Craniofac. Res. 14 (2011) 206–212, doi:10.1111/j.1601-6343.2011.01525.x.

[32] L. Keilig, M. Drolshagen, K.L. Tran, I. Hasan, S. Reimann, J. Deschner, K.T. Brinkmann, R. Krause, M. Favino, C. Bourauel, In vivo measurements and numerical analysis of the biomechanical characteristics of the human periodontal ligament, Ann. Anat. - Anat. Anzeiger. 206 (2016) 80–88, doi:10.1016/j.aanat.2015.08.004.

[33] B. Xu, Y. Wang, Q. Li, Modeling of damage driven fracture failure of fiber post-restored teeth, J. Mech. Behav. Biomed. Mater. 49 (2015) 277–289, doi:10.1016/j.jmbbm.2015.05.006.

[34] R.W. Ogden, Large deformation isotropic elasticity: on the correlation of theory and experiment for compressible rubberlike solids, Proc. R. Soc. A Math. Phys. Eng. Sci. 328 (1972) 567–583, doi:10.1098/rspa.1972.0096.

[35] L.A. Weinberg, Temporomandibular joint function and its effect on concepts of occlusion, J. Prosthet. Dent. 35 (1976) 553–566, doi:10.1016/0022-3913(76)90051-2.

[36] W.H. Douglas, R.L. Sakaguchi, R. DeLong, Frictional effects between natural teeth in an artificial mouth, Dent. Mater. 1 (1985) 115–119, doi:10.1016/S0109-5641(85)80040-3.

[37] M. Farella, S. Palla, S. Erni, A. Michelotti, L.M. Gallo, Masticatory muscle activity during deliberately performed oral tasks, Physiol. Meas. 29 (2008) 1397–1410, doi:10.1088/0967-3334/29/12/004.

[38] A.C. Freitas, E.P. Rocha, P.H. dos Santos, C.-C. Ko, M. Martín, E.O. de Almeida, Mechanics of the maxillary central incisor. Influence of the periodontal ligament represented by beam elements., Comput. Methods Biomech. Biomed. Engin. 13 (2010) 515–521, doi:10.1080/10255840903273175.

[39] A. Oppenheim, Human tissue response to orthodontic intervention of short and long duration, Am. J. Orthod. Oral Surg. 28 (1942) 263–301, doi:10.1016/S0096-6347(42)90492-7.

[40] A. Hohmann, U. Wolfram, M. Geiger, A. Boryor, C. Kober, C. Sander, F.G. Sander, Correspondences of hydrostatic pressure in periodontal ligament with regions of root resorption: a clinical and a finite element study of the same human teeth, Comput. Methods Programs Biomed. 93 (2009) 155–161, doi:10.1016/j.cmpb.2008.09.004.

[41] I.A.V.P. Poiate, A.B. Vasconcellos, R.B. Santana, E. Poiate Jr, Three-dimensional stress distribution in the human periodontal ligament in masticatory, parafunctional, and trauma loads: finite element analysis., J. Periodontol. 80 (2009) 1859–1867, doi:10.1902/jop.2009.090220.

[42] P. Rygh, P. Brudvik, Root resorption and new wire qualities, Eur. J. Orthod. 15 (1993) 343.

[43] F. Weiland, Constant versus dissipating forces in orthodontics: the effect on initial tooth movement and root resorption, Eur. J. Orthod. 25 (2003) 335–342.

[44] T. Van Eijden, Three-dimensional analyses of human bite-force magnitude and moment, Arch. Oral Biol. 36 (1991) 535–539.

[45] J.D. Lin, H. Özcoban, J.P. Greene, A.T. Jang, S.I. Djomehri, K.P. Fahey, L.L. Hunter, G.A. Schneider, S.P. Ho, Biomechanics of a bone–periodontal ligament–tooth fibrous joint, J. Biomech. 46 (2013) 443–449.

[46] Y. Hattori, C. Satoh, T. Kunieda, R. Endoh, H. Hisamatsu, M. Watanabe, Bite forces and their resultants during forceful intercuspal clenching in humans, J. Biomech. 42 (2009) 1533–1538, doi:10.1016/j.jbiomech.2009.03.040.

[47] B. Koos, A. Godt, C. Schille, G. Göz, Precision of an instrumentation-based method of analyzing occlusion and its resulting distribution of forces in the dental arch, J. Orofac. Orthop. / Fortschritte Der Kieferorthopädie 71 (2010) 403–410, doi:10.1007/s00056-010-1023-7.

[48] K. Francová, M. Eber, J. Zapletalová, Functional occlusal patterns during lateral excursions in young adults, J. Prosthet. Dent. 113 (2015) 571–577, doi:10.1016/j.prosdent.2014.12.004.

[49] D. Vollmer, C. Bourauel, K. Maier, A. Jäger, Determination of the centre of resistance in an upper human canine and idealized tooth model, Eur. J. Orthod. 21 (1999) 633–648, doi:10.1093/ejo/21.6.633.

[50] H.T. Shillingburg, D.A. Sather, E.L. Wilson, J.R. Cain, D.L. Mitchell, L.J. Blanco, J.C. Kessler, Fundamentals of Fixed Prosthodontics (2012).

[51] C.-L. Lin, J.-C. Wang, Nonlinear finite element analysis of a splinted implant with various connectors and occlusal forces, Int. J. Oral Maxillofac. Implants 18 (2003).

[52] S.F. Rosenstiel, M.F. Land, J. Fujimoto, Contemporary Fixed Prosthodontics-E–Book, Elsevier Health Sciences, 2015.

[53] W.W. Hallmon, Occlusal trauma: effect and impact on the periodontium, Ann. Periodontol. 4 (1999) 102–108, doi:10.1902/annals.1999.4.1.102.

[54] Z. Liao, J. Chen, W. Li, M.A. Darendeliler, M. Swain, Q. Li, Biomechanical investigation into the role of the periodontal ligament in optimising orthodontic force: a finite element case study, Arch. Oral Biol. 66 (2016) 98–107.

[55] B. Melsen, Tissue reaction to orthodontic tooth movement–a new paradigm, Eur. J. Orthod. 23 (2001) 671–681 doi:11890063.

[56] R. Razaghi, H. Biglari, A. Karimi, Dynamic finite element simulation of dental prostheses during chewing using muscle equivalent force and trajectory approaches, J. Med. Eng. Technol. 41 (2017) 314–324, doi:10.1080/03091902.2017.1299231.

[57] J. Żmudzki, K. Panek, G. Chladek, M. Adamiak, P. Lipinski, Finite element analysis of adolescent mandible fracture occurring during accidents, (2018).

[58] L. Borák, Z. Florian, S. Bartáková, P. Prachár, N. Murakami, M. Ona, Y. Igarashi, N. Wakabayashi, Bilinear elastic property of the periodontal ligament for simulation using a finite element mandible model, Dent. Mater. J. 30 (2011) 448–454, doi:10.4012/dmj.2010-170.